

Orbital Fulde-Ferrell pairing state in moiré Ising superconductors

Ying-Ming Xie^{1,*} and K. T. Law^{1,†}

¹*Department of Physics, Hong Kong University of Science and Technology, Clear Water Bay, Hong Kong, China*
(Dated: June 13, 2023)

In this work, we study superconducting moiré homobilayer transition metal dichalcogenides where the Ising spin-orbit coupling (SOC) is much larger than the moiré bandwidth. We call such non-centrosymmetric superconductors, moiré Ising superconductors. Due to the large Ising SOC, the depairing effect caused by the Zeeman field is negligible and the in-plane upper critical field (B_{c2}) is determined by the orbital effects. This allows us to study the effect of large orbital fields. Interestingly, when the applied in-plane field is larger than the conventional orbital B_{c2} , a finite-momentum pairing phase would appear which we call the orbital Fulde-Ferrell (FF) state. In this state, the Cooper pairs acquire a net momentum of $2q_B$ where $2q_B = eBd$ is the momentum shift caused by the magnetic field B and d denotes the layer separation. This orbital field-driven FF state is different from the conventional FF state driven by Zeeman effects in Rashba superconductors. Remarkably, we predict that the FF pairing would result in a giant superconducting diode effect under electric gating when layer asymmetry is induced. An upturn of the B_{c2} as the temperature is lowered, coupled with the giant superconducting diode effect, would allow the detection of the orbital FF state.

Introduction.—Since the discovery of correlated insulating states and unconventional superconductivity in twisted bilayer graphene [1, 2], moiré superlattices have become important platforms for studying correlated physics, superconductivity, and topological states [3]. Recently, these studies have been extended to a new type of moiré materials based on transition metal dichalcogenides (TMD) [4–23]. Notably, the WSe₂ moiré superlattice further shows a possible signature of superconductivity, in which the resistance drops to zero at a critical temperature of about 1 to 3K [6, 16]. Importantly, superconductivity appears when the Fermi energy is near the valence band top of WSe₂ such that the Ising spin-orbit coupling (SOC) is exceedingly large (in the order of hundreds of meV [24]). The Ising SOC, which pins electron spins at opposite momentum to opposite (out-of-plane) directions [25–27], strongly suppresses the effect of in-plane Zeeman field and enhances in-plane upper critical field B_{c2} [26–41]. Due to the large Ising SOC, the Zeeman depairing effect of the magnetic field can be ignored and the superconductivity of the moiré bilayer can only be suppressed by the orbital effects.

In this work, we study the role of Ising SOC in superconducting TMDs with moiré bands. Specifically, we show that in-plane B_{c2} of the superconducting states goes beyond the Pauli limit [42, 43] but the in-plane B_{c2} is limited by the orbital effect instead of the Zeeman effect. Moreover, we show that the moiré Ising superconductor can be driven to a finite-momentum pairing state at low temperatures by the orbital effects of the magnetic field. Using realistic parameters of twisted bilayer TMDs, we find that the nature of this finite-momentum tends to be a $2q_B$ -Fulde-Ferrell (FF) pairing state [44], in which

Cooper pairs at both layers carry a finite-momentum around $2q_B$ perpendicular to applied fields. The phase transition from the conventional pairing to the finite-momentum pairing can be detected by the temperature dependence of the upper critical field. Interestingly, we predict a giant superconducting diode effect induced by the $2q_B$ -FF pairing under electric gating. The combination of B_{c2} and the diode effect would provide strong evidence of the novel orbital FF state.

Model.—To study the properties of moiré Ising superconductors, we start with a continuum model of twisted homobilayer TMD with Ising SOC and external magnetic fields [5]. We focus on homobilayer TMDs with AA stacking. The lattice constant of each monolayer is denoted by a_0 . The top layer and the bottom layer are rotated by an angle of $\theta/2$ and $-\theta/2$ respectively with respect to one of the transition metal sites (see Fig. 1(a)). The crystal point group symmetry is D_3 , which is generated by a two-fold rotation C_{2y} along the y -axis and a three-fold rotation C_{3z} along the z -axis. It is important to note that inversion symmetry is broken in the moiré bilayer TMD such that the superconducting state can be different from the centrosymmetric bilayer TMD studied in Ref.[45].

The moiré superlattice, which has a moiré lattice constant of $L_M = a_0/\sin\theta$, folds the energy bands and gives rise to the moiré Brillouin. The moiré bands under a finite in-plane magnetic field are described by the Hamiltonian

$$H_\xi(\mathbf{r}) = \begin{pmatrix} h_b(\mathbf{r}) & \hat{T}(\mathbf{r}) \\ \hat{T}^\dagger(\mathbf{r}) & h_t(\mathbf{r}) \end{pmatrix}. \quad (1)$$

where $\xi = \pm$ is the valley index for $\pm\mathbf{K}$ valley. Here the Hamiltonian of each individual layer is given by

$$h_l(\mathbf{r}) = -\frac{1}{2m^*}(\hat{\mathbf{p}} + \mathbf{q}_B\tau_z - \xi\mathbf{K}_l)^2 - \mu + \Omega_\xi^{(l)}(\mathbf{r}) - \xi\beta_{so}s_z + u_B\mathbf{B} \cdot \mathbf{s}, \quad (2)$$

*ymxie@ust.hk

†phlaw@ust.hk

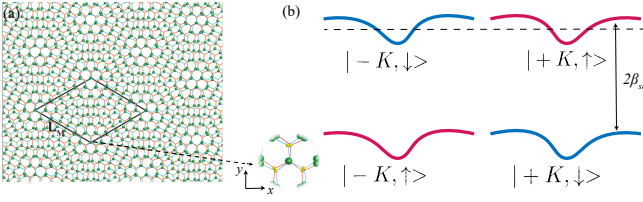


FIG. 1: (a) The lattice structure of a twisted homobilayer TMD. The moiré unit cell is highlighted with L_M as the moiré lattice constant. (b) A schematic plot of the top moiré band of spin-up state and spin-down state at two valleys. Here, $2\beta_{so}$ labels the spin-splitting induced by the Ising SOC.

where $l = t(b)$ labels the top (bottom) layer, m^* denotes the effective mass of valence band, μ is the chemical potential, and τ_i and s_i are Pauli matrices defined in layer and spin space, respectively. The β_{so} characterizes the strength of Ising SOC. The orbital effect of an external magnetic field introduces a momentum shift $q_B = |\mathbf{q}_B| = eBd/2$ with $\mathbf{q}_B = e\mathbf{A}$ and $\mathbf{A} = \frac{1}{2}d\mathbf{B} \times \hat{\mathbf{z}}$ as the chosen gauge potential, where \mathbf{B} denotes the in-plane external magnetic field, d denotes the interlayer distance, e is the electron charge. The Zeeman effect of the external magnetic field is captured by the last term, where the g factor is taken to be 2 and u_B denotes the Bohr magneton. $\Omega_\xi^{(l)}(\mathbf{r})$ is the intralayer moiré potential, and $\hat{T}(\mathbf{r})$ is the interlayer moiré potential. The detailed form of moiré potentials and the model parameters adopted from Ref. [9] are presented in Supplementary Material (SM) Sec. I.

We describe the superconducting twisted homobilayer TMD by a mean-field Hamiltonian, which is written as

$$H_{MF}(\mathbf{r}) = H(\mathbf{r}) + \sum_{\xi} \Psi_{\xi}^{\dagger}(\mathbf{r}) \hat{\Delta}(\mathbf{r}) \Psi_{-\xi}^{\dagger}(\mathbf{r}) + \text{H.c.} \quad (3)$$

Here the moiré Hamiltonian

$$H(\mathbf{r}) = \sum_{\xi} \int d\mathbf{r} \Psi_{\xi}^{\dagger}(\mathbf{r}) \mathcal{H}_{\xi}(\mathbf{r}) \Psi_{\xi}(\mathbf{r}) \quad (4)$$

and $\Psi_{\xi}(\mathbf{r}) = (\psi_{\xi b\uparrow}, \psi_{\xi b\downarrow}, \psi_{\xi t\uparrow}, \psi_{\xi t\downarrow})^T$ denotes a four-component electron annihilation operator. The pairing matrix $\hat{\Delta}(\mathbf{r})$ is represented in the layer and spin space. Due to the layered structure, we expect the pairings to be within electrons of the same layer which can be classified with irreducible representations of D_3 point group (see SM Sec. I [46]). The favoured pairing form is determined by the microscopic interaction. In this work, for illustrative purposes, we consider the two conventional gapped intralayer pairings: $\hat{\Delta}_{A_1} = \Delta i s_y$ and $\hat{\Delta}_{A_2} = \Delta i \tau_z s_y$, where A_1, A_2 label the irreducible representations of D_3 . Here, we consider both A_1 and A_2 pairings as they would generally be mixed by in-plane magnetic fields in the case of finite-momentum pairings.

The enhanced in-plane upper critical field B_{c2} .— The in-plane B_{c2} of the moiré Ising superconductor can be

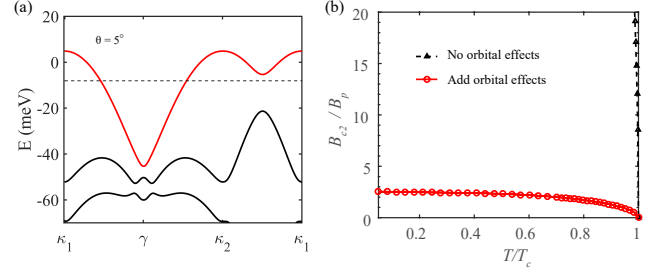


FIG. 2: (a) The moiré bands of a homobilayer TMD with twist angle $\theta = 5^\circ$, where the top moiré bands are highlighted in red. (b) The in-plane upper critical field B_{c2} (in units of Pauli limit $B_p \approx 1.86T_c$) as a function of temperature (in units of the zero-field critical temperature) with (in red) and without (in blue) orbital effects of the magnetic field. We set $T_c = 1$ K and fix the chemical potential at $\nu \approx -0.6$ (the black dashed line in (a) in (b)).

obtained from the linearized gap equation

$$U_0 \chi_s(\mathbf{q}, \mathbf{B}, T) = 1. \quad (5)$$

Here, U_0 denotes the interaction strength that stabilizes $A_{1(2)}$ -pairing, \mathbf{q} is to take account of the possible finite pairing momentum, T is the temperature and the superconducting susceptibility $\chi_s(\mathbf{q}, \mathbf{B}, T)$, in general, is given by the maximal eigenvalue of the pairing susceptibility matrix

$$\hat{\chi}(\mathbf{q}, \mathbf{B}, T) = \begin{pmatrix} \chi_{11}(\mathbf{q}, \mathbf{B}, T) & \chi_{12}(\mathbf{q}, \mathbf{B}, T) \\ \chi_{21}(\mathbf{q}, \mathbf{B}, T) & \chi_{22}(\mathbf{q}, \mathbf{B}, T) \end{pmatrix}. \quad (6)$$

The susceptibility matrix is expressed in the $\hat{\Delta}(\mathbf{q}) = (\Delta_{A_1}(\mathbf{q}), \Delta_{A_2}(\mathbf{q}))^T$ space. More details of the calculations for the pairing susceptibility and the B_{c2} from the Hamiltonian $H_0(\mathbf{p}, \mathbf{B})$ can be found in SM Sec. VI. To be specific, we would fix the filling at $\nu \approx -0.6$ in our calculations and set the field direction along x -direction. In general, a three-fold anisotropy would be expected for the upper critical field. In the main text, we set the twist angle $\theta = 5^\circ$, near where the possible signature of superconductivity would appear in the experiment [6].

The calculated in-plane B_{c2} of the zero-momentum pairing with $\mathbf{q} = 0$ is shown in Fig. 2. Figure 2(a) displays the corresponding moiré energy bands at K valley, where the spin of the top moiré band that contributes to the superconductivity (in red) is fully polarized by the Ising SOC. In this case, the in-plane critical magnetic field B_{c2} (in the unit of the Pauli limit B_p) versus critical temperature T (in units of zero-field critical temperature T_c) curves are plotted in Fig. 2(b), where the orbital effects are present or absent according to Eq. (2). When the orbital effects are artificially turned off while the Zeeman effects are included, it can be seen that the superconducting critical temperature is almost insensitive to the external fields due to the strong Ising SOC. In contrast, the in-plane B_{c2} would ultimately be limited to several B_p when orbital effects are included (red line).

This stands in sharp contrast to superconducting MoS₂ and NbSe₂ where the depairing due to the paramagnetic effect is dominant because of the much smaller Ising SOC at the Fermi energy in these materials.

To estimate the magnitude of the resulting orbital effect limited B_{c2} , we can construct a phenomenological GL free energy theory by taking the order parameter of top and bottom layer to be $\Delta_t \equiv |\Delta|e^{i\varphi_t}$ and $\Delta_b \equiv |\Delta|e^{i\varphi_b}$, respectively. The Ginzburg-Landau (GL) free energy that captures our system can be written as (see SM Sec.V for more details):

$$\mathcal{F}(|\Delta|) = -(\alpha_0 - \alpha_1(B))|\Delta|^2 + \frac{\beta_0}{2}|\Delta|^4 + \lambda_J(1 - \cos(\varphi_t - \varphi_b))|\Delta|^2. \quad (7)$$

Here, $\alpha_0 \propto (T_c - T)$ and β_0 are the GL coefficients, $\alpha_1(B)$ to the second order can be approximated as $\alpha_1(B) = \Lambda q_B^2$. Λ depends on the electron effective mass and interlayer coupling. λ_J denotes the Josephson coupling strength between two layers. As expected, the critical field B_{c2} for zero-momentum pairing is determined by the A_1 pairing, where $\varphi_t = \varphi_b$ to minimize the Josephson coupling energy. According to the coefficient of $|\Delta|^2$, the upper critical field is now estimated as

$$B_c = \sqrt{\frac{4\alpha_0}{e^2 d^2 \Lambda}}. \quad (8)$$

Therefore, the orbital effect limited $B_{c2} \propto \sqrt{T_c - T}$ is mainly determined by the effective mass and thickness. Note that the effective mass strongly depends on the twist angle. As shown in SM Sec. III, the in-plane B_{c2} can be enhanced prominently when we artificially decrease the twist angle.

Orbital Fulde-Ferrell pairing state.— Next, we study the case of finite-momentum pairings with $\mathbf{q} \neq 0$ induced by the orbital effects of magnetic fields. The stabilized finite-momentum pairing is expected to be $\mathbf{q} = (0, q)$, as the orbital motion of electrons is perpendicular to the in-plane magnetic fields. To find the robust q driven by the in-plane magnetic fields, we display the critical field B_c as a function of q in Fig. 3(a) at various temperatures with $T = (0.9, 0.5, 0.1)T_c$. Here, we have used the magnitude of the momentum shift $q_B = |\mathbf{q}_B|$ as defined in Eq. (2) as a natural unit for the pairing momentum q . The robust finite-momentum pairing can be determined by the one with q that maximizes the critical field B_{c2} . Notably, although the zero-momentum pairing $q = 0$ is favored near the critical temperature, a prominent $q \approx \pm 2q_B$ pairing becomes favorable at low temperatures. Figure 3(b) displays the superconducting pairing χ_s versus B curve at $q = 0$ and $|q| = 2q_B$. It clearly shows that the finite-momentum pairing state with $|q| = 2q_B$ exhibits a higher B_{c2} than the zero-momentum pairing state. This $2q_B$ finite-momentum pairing can be understood from the momentum shift induced by orbital effects. The momentum of electrons at two opposite valleys, which would pair together, obtains the same q_B momentum shift according to Eq. (2).

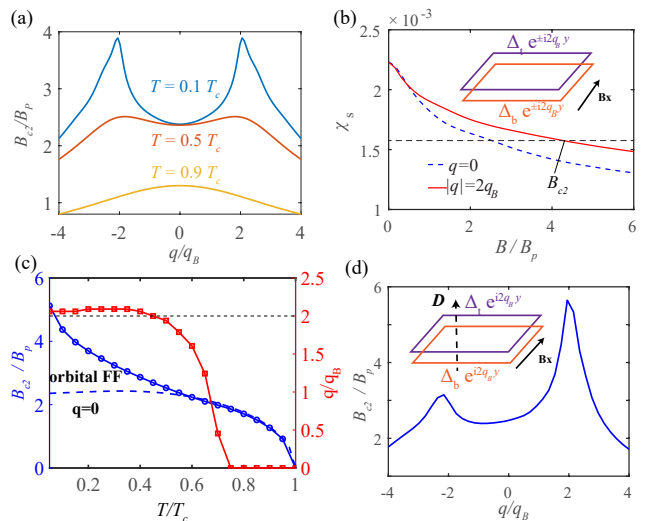


FIG. 3: (a) The in-plane B_{c2} versus pairing momentum q (in units of q_B) at various temperatures $T = 0.1T_c, 0.5T_c, 0.9T_c$. (b) The superconducting pairing susceptibility $\chi_s(q = 0)$ and $\chi_s(q = 2q_B)$ versus B , obtained from diagonalizing the pairing susceptibility matrix. The inset schematically plots the FF pairing with $q_y = 2q_B$ driven by an in-plane field B_x . (c) The left axis shows the B_{c2} versus T curve for finite-momentum q pairing (solid blue line) and zero-momentum pairing ($q = 0$), while the right axis (red line) shows the corresponding favorable pairing momentum q (in units of q_B) as a function of temperature. (d) The B_{c2} versus T curve upon a finite out-of-plane displacement field D . The inset schematically represents the $2q_B$ -FF pairing under finite out-of-plane displacement fields D .

To understand the nature of this $2q_B$ -finite-momentum pairing, we can check the finite-momentum pairing susceptibility $\chi_{ij}(q = 2q_B)$ versus B . The stabilized pairing form could be obtained from the pairing susceptibility matrix Eq. (6), which can be written as

$$\Delta(\mathbf{r}) = \sum_{\mathbf{q}} \Delta_{\mathbf{q}} \left(\cos \frac{\theta_{\mathbf{q}}}{2} + \sin \frac{\theta_{\mathbf{q}}}{2} \tau_z \right) i \sigma_y e^{i\mathbf{q} \cdot \mathbf{r}} \quad (9)$$

Here, $(\cos \frac{\theta_{\mathbf{q}}}{2}, \sin \frac{\theta_{\mathbf{q}}}{2})^T$ represents the corresponding eigenvector of χ_s with $\theta_{\mathbf{q}} = \arcsin \frac{\chi_{12}}{\sqrt{(\chi_{11} - \chi_{22})^2/4 + \chi_{12}^2}}$. Due to the presence of finite interlayer coupling, the resulting finite-momentum pairing susceptibility $\chi_{11} - \chi_{22} \gg \chi_{12}$ so that $\theta_{\mathbf{q}} \approx 0$ (SM Sec. III). As a result, according to Eq. (9), the stabilized pairing form behaves as a FF pairing, which can be parameterized as $\Delta(\mathbf{r}) = |\Delta|e^{i\mathbf{q} \cdot \mathbf{r}}$ or $\Delta(\mathbf{r}) = |\Delta|e^{-i\mathbf{q} \cdot \mathbf{r}}$ with $\mathbf{q} = (0, 2q_B)$ (see an illustration in the inset of Fig. 3). We denote these two pairings as $\pm 2q_B$ -FF pairings. Note that although these two pairings with opposite pairing momentum are nearly degenerate, the mixing of them is not favorable according to the GL free energy analysis up to the fourth order (see SM Sec. V). Moreover, according to a phenomenological GL analysis in Sec. V, the interlayer coupling would increase the kinetic energy of

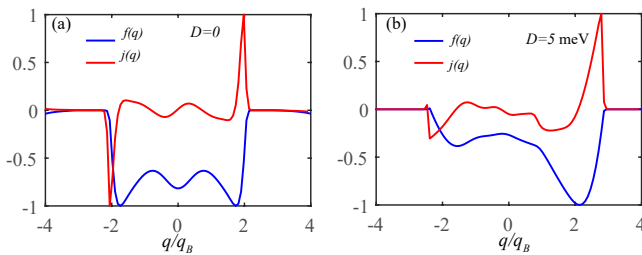


FIG. 4: (a) and (b) show the free energy $f(q)$ and supercurrent $j(q)$ normalized to $[-1, 1]$ without displacement fields ($D = 0$ meV) and with a finite displacement field ($D = 5$ meV) respectively. Here the temperature $T = 0.1T_c$, and $B = 3B_p$ and $B = 2.5B_p$ for (a) and (b), respectively. In (a), the maximum magnitudes of $j(q)$ are the same in the positive and negative directions. This indicates the absence of the superconducting diode effect. In (b), the maximum magnitudes of $j(q)$ are different for currents flowing in opposite directions, indicating the presence of the superconducting diode effect.

the superconductor under in-plane magnetic fields due to the canonical momentum mixing between the two layers. On the other hand, the $2q_B$ -FF pairing would lower this energy, which could make it more favorable than the zero-momentum pairing.

To obtain the B - T phase diagram, we plot the critical B_{c2} (left axis, solid blue) and the corresponding stabilized $\mathbf{q} = (0, q)$ (right axis, red) as a function of temperature T in Fig. 3(c). The finite-momentum pairing ($q > 0$) is seen to emerge at temperature $T \approx 0.75T_c$, near where the B_c - T curve exhibits an upturn at the phase transition. Notably, the momentum shifts q would saturate and the previously discussed $2q_B$ -FF pairings emerge at low temperatures $T \lesssim 0.5T_c$. The finite-momentum pairing phase region, the boundary of which is roughly given by the B_c - T curve with $q = 0$ and finite q , is highlighted in Fig. 3(c). It can be seen that the $2q_B$ -FF state can be stabilized with a temperature $T \lesssim 0.5T_c$ and a magnetic field B roughly higher than $2B_p$.

Finally, we point out that the degeneracy between $+2q_B$ -FF pairing and $-2q_B$ -FF pairing can be lifted extrinsically by out-of-plane displacement fields D , which induces layer asymmetry. As shown in Fig. 3(d), when an out-of-plane displacement field $D = 5$ meV is applied, the B_{c2} of $2q_B$ finite-momentum pairing becomes much higher than the B_{c2} of the $-2q_B$ pairing, implying that $+2q_B$ -FF pairing would be the favorable finite-momentum pairing under a large in-plane magnetic field. Note that in the experiment, superconductivity of twisted bilayer TMDs occurs in the presence of a displacement field.

Gate-tunable superconducting diode effect.— Next, we demonstrate a gate-tunable superconducting diode effect based on the proposed $2q_B$ -FF pairing in moiré Ising superconductors. The superconducting diode effect is characterized by the critical current difference between currents flowing in opposite directions: $\Delta j_c =$

$(j_{c,+} - |j_{c,-}|)/(j_{c,+} + |j_{c,-}|)$ [47–51], where the $+$ and $-$ signs denote the opposite current directions respectively.

To demonstrate this, we can calculate the supercurrent $j(\mathbf{q})$ from the free energy [52]

$$f_s(\Delta, \mathbf{q}) = \frac{|\Delta|^2}{U_0} - \frac{1}{\beta} \sum_{\mathbf{k}, n} \ln(1 + e^{-\beta \epsilon_{n\mathbf{q}}(\mathbf{k})}). \quad (10)$$

where $\beta = 1/k_B T$, $\epsilon_{n\mathbf{q}}(\mathbf{k})$ is the quasi-particle energy of the finite-momentum Bogoliubov-de Gennes (BdG) Hamiltonian (see SM Sec. IV [46] for more details). The supercurrent $j(\mathbf{q})$ can be obtained by $j(\mathbf{q}) = 2 \frac{\partial f(\mathbf{q})}{\partial \mathbf{q}}$, where $f(\mathbf{q})$ is the lowest free energy at each pairing momentum \mathbf{q} and is given by minimizing the free energy $f_s(\Delta, \mathbf{q}) - f_n$ (note $f_n \equiv f_s(\Delta = 0)$ is the normal state free energy) with respect to Δ . Here, we consider the current direction to be along y -direction so that we can denote $\mathbf{q} = (0, q)$.

The landscape of the minimized free energy $f(q)$ (blue line) and the corresponding supercurrent $j(q)$ (red line) in the case without displacement fields ($D = 0$) and with displacement fields ($D = 5$ meV) are plotted in Fig. 4. Here a large in-plane magnetic field ($B/B_p = 3$ and $B/B_p = 2.5$ for (a) and (b), respectively), and a temperature $T = 0.1T_c$ are adopted so that the system is deep in the FF pairing state. It is important to note that Ising SOC is very essential here. Without Ising SOC, the superconductivity could have been killed by the paramagnetic effect before reaching the FF state. Without displacement fields (Fig. 4(a)), the free energy of q near $\pm 2q_B$ is lower than $q = 0$ under a large B . In other words, $\pm 2q_B$ -FF pairing would be stabilized, being consistent with the previous linearized gap equation calculation. However, the diode effect is absent ($\Delta j_c = 0$) in this case (Fig. 4(a)). As shown in Fig. 4(b), the diode effect becomes finite at finite displacement fields ($D = 5$ meV). Notably, the resulting $\Delta j_c \approx 53\%$ is much larger than the one proposed in superconductors with Rashba SOC [48]. This giant superconducting diode effect originates from the lifting of the degeneracy between $2q_B$ -FF pairing and $-2q_B$ -FF pairing by the displacement field, which enables a highly asymmetric free energy configuration as shown in Fig. 4(b). The implementation of an electric gate-tunable superconducting diode effect is generally difficult in previous systems [47, 53, 54], as the high electron density hinders the gate-controllability. The giant gate-tunable superconducting diode effect in the present system is potentially useful for dissipationless electronics, superconducting circuits and superconducting computing devices.

Discussion.— It is worth noting that the pairing form $\Delta(\mathbf{r})$ can be changed if the interlayer coupling strength can be tuned. For example, as shown in SM Sec. VI, we obtained a layer-antisymmetric FF pairing analytically, where $\Delta_t = |\Delta|e^{i\mathbf{q}\cdot\mathbf{r}}$ and $\Delta_b = |\Delta|e^{-i\mathbf{q}\cdot\mathbf{r}}$ with $\mathbf{q} = (0, 2q_B)$, in the case without twisting and in the weak interlayer coupling limit. We note that this exotic pairing has been proposed in centrosymmetric AB

stacked bilayer TMDs without twisting previously [45]. This layer-antisymmetric FF pairing is energetically not favored in our case due to the stronger interlayer coupling strength, which increases the Josephson coupling energy. The orbital FF pairings we find would not afford such Josephson coupling energy and are particularly allowed by noncentrosymmetric superconductors.

In conclusion, we have proposed an intriguing non-centrosymmetric superconductor—moiré Ising superconductor, in which the Ising SOC is dominant over moiré bandwidth and can be readily realized in superconducting moiré TMDs. We have highlighted that moiré Ising superconductors are wonderful platforms for exploring novel superconducting effects, including orbital magnetic field-driven finite-momentum pairing state and

gate-tunable superconducting diode effects. In principle, our theory for the orbital FF pairing state can also be applied to some other non-twisted superconducting materials with inversion broken and giant Ising SOC.

Acknowledgments.—K.T.L. acknowledges the support of the Ministry of Science and Technology, China, and HKRGC through Grants No. 2020YFA0309600, No. RFS2021-6S03, No. C6025-19G, No. AoE/P-701/20, No. 16310520, No. 16310219, No. 16307622 and No. 16309718. Y.M.X. acknowledges the support of HKRGC through PDFS2223-6S01.

Note.— After drafting this work, we were informed by Justin Ye that the orbital-field-driven finite-momentum pairing state might have been observed in multilayer 2H-NbSe₂ [55].

-
- [1] Y. Cao, V. Fatemi, A. Demir, S. Fang, S. L. Tomarken, J. Y. Luo, J. D. Sanchez-Yamagishi, K. Watanabe, T. Taniguchi, E. Kaxiras, R. C. Ashoori, and P. Jarillo-Herrero, *Nature* **556**, 80 (2018).
- [2] Y. Cao, V. Fatemi, S. Fang, K. Watanabe, T. Taniguchi, E. Kaxiras, and P. Jarillo-Herrero, *Nature* **556**, 43 (2018).
- [3] E. Y. Andrei, D. K. Efetov, P. Jarillo-Herrero, A. H. MacDonald, K. F. Mak, T. Senthil, E. Tutuc, A. Yazdani, and A. F. Young, *Nature Reviews Materials* **6**, 201 (2021).
- [4] F. Wu, T. Lovorn, E. Tutuc, and A. H. MacDonald, *Phys. Rev. Lett.* **121**, 026402 (2018).
- [5] F. Wu, T. Lovorn, E. Tutuc, I. Martin, and A. H. MacDonald, *Phys. Rev. Lett.* **122**, 086402 (2019).
- [6] L. Wang, E.-M. Shih, A. Ghiotto, L. Xian, D. A. Rhodes, C. Tan, M. Claassen, D. M. Kennes, Y. Bai, B. Kim, K. Watanabe, T. Taniguchi, X. Zhu, J. Hone, A. Rubio, A. N. Pasupathy, and C. R. Dean, *Nature Materials* **19**, 861 (2020).
- [7] Z. Zhang, Y. Wang, K. Watanabe, T. Taniguchi, K. Ueno, E. Tutuc, and B. J. LeRoy, *Nature Physics* **16**, 1093 (2020).
- [8] Y. Tang, L. Li, T. Li, Y. Xu, S. Liu, K. Barmak, K. Watanabe, T. Taniguchi, A. H. MacDonald, J. Shan, and K. F. Mak, *Nature* **579**, 353 (2020).
- [9] E. C. Regan, D. Wang, C. Jin, M. I. Bakti Utama, B. Gao, X. Wei, S. Zhao, W. Zhao, Z. Zhang, K. Yumigeta, M. Blei, J. D. Carlström, K. Watanabe, T. Taniguchi, S. Tongay, M. Crommie, A. Zettl, and F. Wang, *Nature* **579**, 359 (2020).
- [10] Y. Xu, S. Liu, D. A. Rhodes, K. Watanabe, T. Taniguchi, J. Hone, V. Elser, K. F. Mak, and J. Shan, *Nature* **587**, 214 (2020).
- [11] X. Huang, T. Wang, S. Miao, C. Wang, Z. Li, Z. Lian, T. Taniguchi, K. Watanabe, S. Okamoto, D. Xiao, S.-F. Shi, and Y.-T. Cui, *Nature Physics* **17**, 715 (2021).
- [12] Y. Zhang, N. F. Q. Yuan, and L. Fu, *Phys. Rev. B* **102**, 201115 (2020).
- [13] C. Jin, Z. Tao, T. Li, Y. Xu, Y. Tang, J. Zhu, S. Liu, K. Watanabe, T. Taniguchi, J. C. Hone, L. Fu, J. Shan, and K. F. Mak, *Nature Materials* (2021), 10.1038/s41563-021-00959-8.
- [14] T. Li, S. Jiang, B. Shen, Y. Zhang, L. Li, Z. Tao, T. Devakul, K. Watanabe, T. Taniguchi, L. Fu, J. Shan, and K. F. Mak, *Nature* **600**, 641 (2021).
- [15] K. F. Mak and J. Shan, *Nature Nanotechnology* **17**, 686 (2022).
- [16] L. An, X. Cai, D. Pei, M. Huang, Z. Wu, Z. Zhou, J. Lin, Z. Ying, Z. Ye, X. Feng, *et al.*, *Nanoscale horizons* .
- [17] Y.-T. Hsu, F. Wu, and S. Das Sarma, *Phys. Rev. B* **104**, 195134 (2021).
- [18] C. Schrade and L. Fu, arXiv e-prints , arXiv:2110.10172 (2021), arXiv:2110.10172 [cond-mat.supr-con] .
- [19] L. Klebl, A. Fischer, L. Classen, M. M. Scherer, and D. M. Kennes, *Phys. Rev. Res.* **5**, L012034 (2023).
- [20] Y.-M. Wu, Z. Wu, and H. Yao, *Phys. Rev. Lett.* **130**, 126001 (2023).
- [21] A. Wietek, J. Wang, J. Zang, J. Cano, A. Georges, and A. Millis, arXiv e-prints , arXiv:2204.04229 (2022), arXiv:2204.04229 [cond-mat.str-el] .
- [22] B. Zhou and Y.-H. Zhang, arXiv e-prints , arXiv:2209.10023 (2022), arXiv:2209.10023 [cond-mat.str-el] .
- [23] M. Bélanger, J. Fournier, and D. Sénéchal, *Phys. Rev. B* **106**, 235135 (2022).
- [24] G.-B. Liu, W.-Y. Shan, Y. Yao, W. Yao, and D. Xiao, *Phys. Rev. B* **88**, 085433 (2013).
- [25] D. Xiao, G.-B. Liu, W. Feng, X. Xu, and W. Yao, *Phys. Rev. Lett.* **108**, 196802 (2012).
- [26] J. M. Lu, O. Zheliuk, I. Leermakers, N. F. Q. Yuan, U. Zeitler, K. T. Law, and J. T. Ye, *Science* **350**, 1353 (2015).
- [27] X. Xi, Z. Wang, W. Zhao, J.-H. Park, K. T. Law, H. Berger, L. Forró, J. Shan, and K. F. Mak, *Nature Physics* **12**, 139 (2016).
- [28] Y. Saito, Y. Nakamura, M. S. Bahramy, Y. Kohama, J. Ye, Y. Kasahara, Y. Nakagawa, M. Onga, M. Tokunaga, T. Nojima, Y. Yanase, and Y. Iwasa, *Nature Physics* **12**, 144 (2016).
- [29] S. C. de la Barrera, M. R. Sinko, D. P. Gopalan, N. Sivadas, K. L. Seyler, K. Watanabe, T. Taniguchi, A. W. Tsen, X. Xu, D. Xiao, and B. M. Hunt, *Nature Communications* **9**, 1427 (2018).
- [30] J. Lu, O. Zheliuk, Q. Chen, I. Leermakers, N. E. Hussey, U. Zeitler, and J. Ye, *Proceedings of the National*

- Academy of Sciences **115**, 3551 (2018).
- [31] Y. Xing, K. Zhao, P. Shan, F. Zheng, Y. Zhang, H. Fu, Y. Liu, M. Tian, C. Xi, H. Liu, J. Feng, X. Lin, S. Ji, X. Chen, Q.-K. Xue, and J. Wang, *Nano Letters* **17**, 6802 (2017).
 - [32] E. Sohn, X. Xi, W.-Y. He, S. Jiang, Z. Wang, K. Kang, J.-H. Park, H. Berger, L. Forró, K. T. Law, J. Shan, and K. F. Mak, *Nature Materials* **17**, 504 (2018).
 - [33] B. T. Zhou, N. F. Q. Yuan, H.-L. Jiang, and K. T. Law, *Phys. Rev. B* **93**, 180501 (2016).
 - [34] W.-Y. He, B. T. Zhou, J. J. He, N. F. Q. Yuan, T. Zhang, and K. T. Law, *Communications Physics* **1**, 40 (2018).
 - [35] Y. Xie, B. T. Zhou, T. K. Ng, and K. T. Law, *Phys. Rev. Research* **2**, 013026 (2020).
 - [36] G. Sharma and S. Tewari, *Phys. Rev. B* **94**, 094515 (2016).
 - [37] S. Ilić, J. S. Meyer, and M. Houzet, *Phys. Rev. Lett.* **119**, 117001 (2017).
 - [38] J. Zhang and V. Aji, *Phys. Rev. B* **94**, 060501 (2016).
 - [39] Y. Nakamura and Y. Yanase, *Phys. Rev. B* **96**, 054501 (2017).
 - [40] Y.-T. Hsu, A. Vaezi, M. H. Fischer, and E.-A. Kim, *Nature Communications* **8**, 14985 (2017).
 - [41] D. Wickramaratne, S. Khmelevskiy, D. F. Agterberg, and I. I. Mazin, *Phys. Rev. X* **10**, 041003 (2020).
 - [42] A. M. Clogston, *Phys. Rev. Lett.* **9**, 266 (1962).
 - [43] B. S. Chandrasekhar, *Applied Physics Letters* **1**, 7 (1962).
 - [44] P. Fulde and R. A. Ferrell, *Phys. Rev.* **135**, A550 (1964).
 - [45] C.-X. Liu, *Phys. Rev. Lett.* **118**, 087001 (2017).
 - [46] See Supplementary material for (i) details for the moiré potential and model parameters; (ii) pairing classifications for twisted bilayer TMD; (iii) extended figures; (iv) the linearized gap equation and free energy for the finite momentum pairing; (v) Ginzburg-Landau Free energy for a bilayer superconductor under in-plane orbital magnetic fields; (vi) the layer anti-symmetric $2q_B$ FF pairing in AA stacking bilayer TMD in weak interlayer coupling limit.
 - [47] F. Ando, Y. Miyasaka, T. Li, J. Ishizuka, T. Arakawa, Y. Shiotani, T. Moriyama, Y. Yanase, and T. Ono, *Nature* **584**, 373 (2020).
 - [48] A. Daido, Y. Ikeda, and Y. Yanase, *Phys. Rev. Lett.* **128**, 037001 (2022).
 - [49] N. F. Q. Yuan and L. Fu, *Proceedings of the National Academy of Sciences* **119**, e2119548119 (2022), <https://www.pnas.org/doi/pdf/10.1073/pnas.2119548119>.
 - [50] J. J. He, Y. Tanaka, and N. Nagaosa, *New Journal of Physics* **24**, 053014 (2022).
 - [51] S. Ilić and F. S. Bergeret, *Phys. Rev. Lett.* **128**, 177001 (2022).
 - [52] Y.-M. Xie, B. T. Zhou, and K. T. Law, *Phys. Rev. Lett.* **125**, 107001 (2020).
 - [53] H. Wu, Y. Wang, Y. Xu, P. K. Sivakumar, C. Pasco, U. Filippozzi, S. S. P. Parkin, Y.-J. Zeng, T. McQueen, and M. N. Ali, *Nature* **604**, 653 (2022).
 - [54] L. Bauriedl, C. Bäuml, L. Fuchs, C. Baumgartner, N. Paulik, J. M. Bauer, K.-Q. Lin, J. M. Lupton, T. Taniguchi, K. Watanabe, C. Strunk, and N. Paradiso, *Nature Communications* **13**, 4266 (2022).
 - [55] P. Wan, O. Zheliuk, N. F. Q. Yuan, X. Peng, L. Zhang, M. Liang, U. Zeitler, S. Wiedmann, N. E. Hussey, T. T. M. Palstra, and J. Ye, *Nature* (2023), 10.1038/s41586-023-05967-z.

Supplementary Material for “Orbital Fulde–Ferrell pairing state in Moiré Ising superconductors”

Ying-Ming Xie,¹ K. T. Law¹

¹*Department of Physics, Hong Kong University of Science and Technology, Clear Water Water Bay, Hong Kong, China*

I. DETAILS FOR THE MOIRÉ POTENTIAL AND MODEL PARAMETERS

In this supplementary material section, we present the detailed form of the moiré potential and the adopted model parameters for the twisted homobilayer TMD in the main text. The intralayer moiré potential is given by

$$\Omega_{\xi s}^{(l)}(\mathbf{r}) = V_{\xi s} \sum_{j=1,3,5} e^{i\xi(\mathbf{g}_j \cdot \mathbf{r} + l\psi_{\xi s})} + h.c., \quad (\text{S1})$$

where $V_{\xi s}$ and $\psi_{\xi s}$ (ξ, s are valley and spin indices), respectively, characterize the amplitude and the shape of intralayer moiré potential, and the moiré reciprocal lattice vectors $\mathbf{g}_i = \frac{4\pi}{\sqrt{3}L_M}(\cos \frac{(i-1)\pi}{3}, \sin \frac{(i-1)\pi}{3})$. The interlayer tunneling moiré potential $\hat{T}(\mathbf{r})$ in main text is given by

$$\begin{aligned} \hat{T}(\mathbf{r}) = & \begin{pmatrix} u_{\xi\uparrow} & u_{\uparrow\downarrow} \\ u_{\downarrow\uparrow} & u_{\xi\downarrow} \end{pmatrix} + \begin{pmatrix} u_{\xi\uparrow} & u_{\uparrow\downarrow}\omega^{-1} \\ u_{\downarrow\uparrow}\omega & u_{\xi\downarrow} \end{pmatrix} e^{-i\xi\mathbf{g}_2 \cdot \mathbf{r}} \\ & + \begin{pmatrix} u_{\xi\uparrow} & u_{\uparrow\downarrow}\omega \\ u_{\downarrow\uparrow}\omega^{-1} & u_{\xi\downarrow} \end{pmatrix} e^{-i\xi\mathbf{g}_3 \cdot \mathbf{r}}, \end{aligned} \quad (\text{S2})$$

with $\omega = e^{i2\pi/3}$.

To roughly capture the relevant energy scale of twisted bilayer TMD, in the calculation, we adopt the model parameters given in ref. [5] in the main text: $1/2m^* = 510.45$ meV, $\beta_{so} = 110.25$ meV. $(V_{+\uparrow}, \psi_{+\downarrow}, u_{+\uparrow}) = (8$ meV, $-89.8^\circ, -8.5$ meV), $(V_{+\downarrow}, \psi_{+\downarrow}, u_{+\downarrow}) = (7.7$ meV, $-88.35^\circ, -6.5$ meV) and $u_{\uparrow\downarrow} = -i5.6$ meV, which are obtained by fitting the first-principle band structure of homobilayer MoTe₂. With the reversal symmetry operation, we have $V_{\pm\uparrow} = V_{\mp\downarrow}, \psi_{\pm\uparrow} = \psi_{\mp\downarrow}, u_{\pm\uparrow} = u_{\mp\downarrow}$.

II. PAIRING CLASSIFICATIONS FOR TWISTED BILAYER TMD

In the absence of displacement fields and external fields, the twisted bilayer TMD respects $\hat{\mathcal{T}} \times D_3$ symmetry. Here, $\hat{\mathcal{T}} = is_y K$ with K as complex conjugate denotes time-reversal symmetry, and D_3 point group symmetry is generated by a three-fold rotational symmetry $C_{3z} = e^{-i\frac{\pi}{3}s_z}$ and an in-plane two-fold rotational symmetry $C_{2y} = -i\tau_x s_y$.

The continuum Hamiltonian for the superconducting part can be written as

$$H_{SC}(\mathbf{r}) = \int d\mathbf{r} \sum_{\xi, l, l', s, s'} \psi_{\xi l s}^\dagger(\mathbf{r}) \hat{\Delta}_{ll', ss'}(\mathbf{r}) \psi_{-\xi l' s'}^\dagger(\mathbf{r}) + \text{H.c.} \quad (\text{S3})$$

Here, $l = t, b$ is the layer indices. We can classify all possible pairings with the irreducible representations of the D_3 point group. This classification is done by noting (i) the pairing matrix transforms as

$$\hat{\mathcal{T}} : \hat{\Delta}(\mathbf{r}) \mapsto s_y \hat{\Delta}^*(\mathbf{r}) s_y \quad (\text{S4})$$

$$g : \hat{\Delta}(\mathbf{r}) \mapsto U^T(g) \hat{\Delta}(g\mathbf{r}) U(g), \quad (\text{S5})$$

where g denotes the symmetry operation C_{3z} and C_{2y} , $U(g)$ is the matrix representation of the symmetry operation g . (ii) Due to the antisymmetric requirement of Cooper pair wave functions, the pairing matrices must satisfy $\hat{\Delta}^T(\mathbf{r}) = -\hat{\Delta}(\mathbf{r})$.

For simplicity, we only take momentum independent pairings into account. There are only six matrices: $s_y, \tau_x s_y, \tau_z s_y, \tau_y, \tau_y s_x, \tau_y s_z$ can couple to the momentum independent pairings. The possible momentum-independent pairings in the layer and spin space can be classified in Table S1. The $\Delta_{A_1,1}, \Delta_{A_2}$ are intralayer singlet pairings and the $\Delta_{A_1,2}, \Delta_{A_1,3}$ are interlayer singlet pairings, while the $\Delta_{E_1}, \Delta_{E_2}$ belonging to a two-dimensional irreducible representation is interlayer triplet pairings.

Supplementary Table 1: Classification of possible s-wave pairings for twisted bilayer TMD with the irreducible representations of D_3 point group in layer and spin space. Here s, τ are Pauli matrices defining in spin and layer space.

| | Rep. | Matrix form γ | Explicit form |
|-------|----------------------------------|--------------------------|---|
| A_1 | $\Delta_{A_1,1}$ | $i s_y$ | $\psi_{-\xi-\mathbf{k},t\uparrow}\psi_{\xi+\mathbf{k},t\downarrow} + \psi_{-\xi-\mathbf{k},b\uparrow}\psi_{\xi+\mathbf{k},b\downarrow}$ |
| | $\Delta_{A_1,2}$ | $i \tau_x s_y$ | $\psi_{-\xi-\mathbf{k},t\uparrow}\psi_{\xi+\mathbf{k},b\downarrow} + \psi_{-\xi-\mathbf{k},b\uparrow}\psi_{\xi+\mathbf{k},t\downarrow}$ |
| | $\Delta_{A_1,3}$ | $\tau_y s_x$ | $\psi_{-\xi-\mathbf{k},t\uparrow}\psi_{\xi+\mathbf{k},b\downarrow} - \psi_{-\xi-\mathbf{k},b\uparrow}\psi_{\xi+\mathbf{k},t\downarrow}$ |
| A_2 | Δ_{A_2} | $i \tau_z s_y$ | $\psi_{-\xi-\mathbf{k},t\uparrow}\psi_{\xi+\mathbf{k},t\downarrow} - \psi_{-\xi-\mathbf{k},b\uparrow}\psi_{\xi+\mathbf{k},b\downarrow}$ |
| E | $\{\Delta_{E_1}, \Delta_{E_2}\}$ | $\{\tau_y, \tau_y s_z\}$ | $\{\psi_{-\xi-\mathbf{k},t\uparrow}\psi_{\xi+\mathbf{k},b\uparrow} + \psi_{-\xi-\mathbf{k},t\downarrow}\psi_{\xi+\mathbf{k},b\downarrow},$ $\psi_{-\xi-\mathbf{k},t\uparrow}\psi_{\xi+\mathbf{k},b\uparrow} - \psi_{-\xi-\mathbf{k},t\downarrow}\psi_{\xi+\mathbf{k},b\downarrow}\}$ |

III. EXTENDED FIGURES

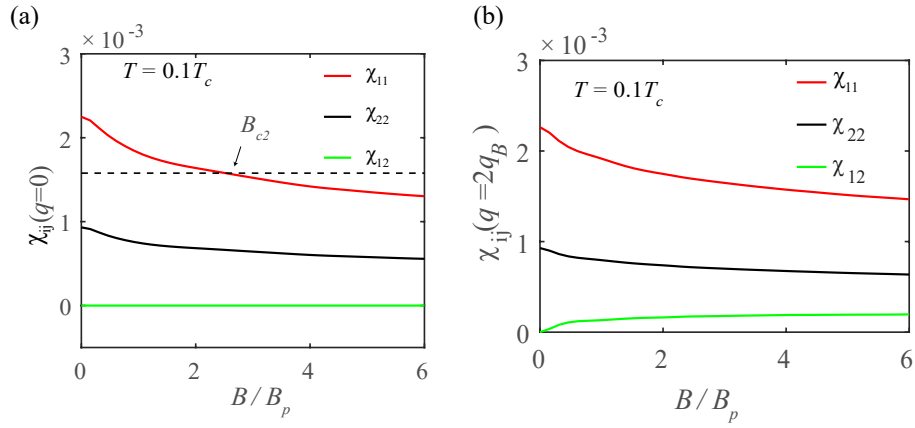


FIG. S1: Pairing susceptibility for A_1 pairing χ_{11} , A_2 pairing, χ_{22} and their mixing χ_{12} . (a) The zero-momentum pairing susceptibility $\chi_{ij}(q=0)$ versus in-plane magnetic fields B . The critical field B_{c2} is highlighted. (b) The finite-momentum pairing susceptibility $\chi_{ij}(q=2q_B)$ versus B . Other parameters are the same as the main text Fig. 2.

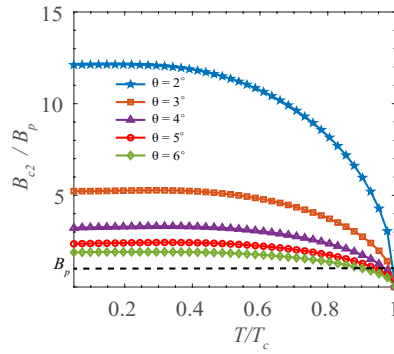


FIG. S2: The in-plane upper critical field B_{c2} versus T (with orbital effects) at various twist angle θ .

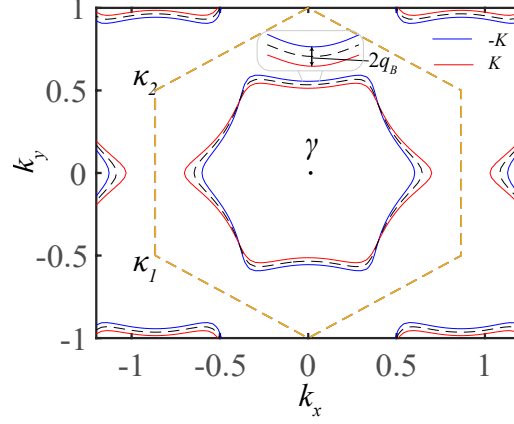


FIG. S3: The Fermi contour between at + K valley (blue) and $-K$ valley (red) under finite magnetic field. The back dashed line labels the Fermi contour in the case without magnetic fields. The brown dashed line labels the boundaries of the Brillouin zone. To make the shifting of the Fermi contour more obvious, we adopt a large in-plane magnetic field $B = 20B_p$. The $2q_B$ momentum shifting between the Fermi contour of K and $-K$ valley is highlighted (see the inset). Note that due to the interlayer hopping, the momentum shifting, in general, is not uniform.

IV. THE LINEARIZED GAP EQUATION AND FREE ENERGY FOR THE FINITE MOMENTUM PAIRING

As presented in the main text, the mean-field Hamiltonian is written as

$$H_{MF}(\mathbf{r}) = \sum_{\xi} \int d\mathbf{r} \Psi_{\xi}^{\dagger}(\mathbf{r}) \mathcal{H}_{\xi}(\mathbf{r}) \Psi_{\xi}(\mathbf{r}) + \sum_{\xi} (\Psi_{\xi}^{\dagger}(\mathbf{r}) \hat{\Delta}(\mathbf{r}) \Psi_{-\xi}^{\dagger}(\mathbf{r}) + \text{H.c.}). \quad (\text{S6})$$

Here, the four-component annihilation operator $\Psi_{\xi}(\mathbf{r}) = (\psi_{\xi b\uparrow}, \psi_{\xi b\downarrow}, \psi_{\xi t\uparrow}, \psi_{\xi t\downarrow})^T$. By directly transforming the continuum superconducting Hamiltonian into momentum space, we obtain

$$H_{MF} = \frac{1}{A} \sum_{\mathbf{p}} \Psi_{\xi}^{\dagger}(\mathbf{p}) [H_0(\mathbf{p})] \Psi_{\xi}(\mathbf{p}) + \frac{1}{A} \sum_{\mathbf{p}', \mathbf{q}} (\Psi_{\xi}^{\dagger}(\mathbf{p} + \frac{\mathbf{q}}{2}) \hat{\Delta}(\mathbf{q}) \Psi_{-\xi}^{\dagger}(-\mathbf{p} + \frac{\mathbf{q}}{2}) + h.c.), \quad (\text{S7})$$

where A is the area of the moiré unit cell, \mathbf{p} is the momentum within the first moiré Brillouin zone, $H_0(\mathbf{p})$ is the moiré Hamiltonian that can be represented a plane wave basis, where the elements can be given by $\langle \mathbf{p} + m\mathbf{g}_2 + n\mathbf{g}_3 | \mathcal{H}_{\xi}(\mathbf{r}) | \mathbf{p} + m'\mathbf{g}_2 + n'\mathbf{g}_3 \rangle$ with m, n as integers, \mathbf{g}_j as moiré wave vectors defined in the main text. The moiré bands are obtained by diagonalizing the moiré Hamiltonian with a finite cut-off on m, n .

The linearized gap equation. We can decompose the pairings into the different channels $\hat{\Delta}(\mathbf{q}) = \sum_{i\mu} \Delta_{i\mu}(\mathbf{q}) \gamma_{i\mu}$ with $\gamma_{i\mu}$ denoting the representation matrix defined in layer and spin space, and the linearize gap equation is given by

$$\Delta_{i\mu}(\mathbf{q}) = V_i \sum_{j\nu} \chi_{ij, \mu\nu}(\mathbf{q}) \Delta_{j\nu}(\mathbf{q}), \quad (\text{S8})$$

where i, j label the representation, μ, ν label the component in this representation, V_i denotes the strength of attractive interaction, \mathbf{q} denotes the finite-momentum pairing of Cooper pairs. The superconductivity susceptibility is given by

$$\chi_{ij, \mu\nu}^{(2)}(\mathbf{q}) = -\frac{1}{\beta} \sum_{i\omega_n, \mathbf{p}} \text{Tr}(\gamma_{i\mu}^{\dagger} G_e(\mathbf{p} + \mathbf{q}/2, i\omega_n) \gamma_{j\nu} G_h(\mathbf{p} - \mathbf{q}/2, i\omega_n)), \quad (\text{S9})$$

where $\beta = 1/k_B T$, the single-particle Green's functions for electrons $G_e(\mathbf{p}, i\omega_n) = (i\omega_n - H_0(\mathbf{p}))^{-1}$ and holes $G_h(\mathbf{p}, i\omega_n) = (i\omega_n + H_0^*(-\mathbf{p}))^{-1}$ with $H_0(\mathbf{p})$ as the moiré Hamiltonian.

By utilizing the eigenstates of $H_0(\mathbf{p})$: $H_0(\mathbf{p}) |u_{a\mathbf{p}}\rangle = E_a(\mathbf{p}) |u_{a\mathbf{p}}\rangle$, $H_0^*(\mathbf{p}) |\nu_{b\mathbf{p}}\rangle = E_b'(\mathbf{p}) |\nu_{b\mathbf{p}}\rangle$ (a and b are band indices), we can further simplify Eq. S9 as

$$\chi_{ij, \mu\nu}^{(2)}(\mathbf{q}) = \int_{\mathbf{p}} \sum_{a,b} O_{a,b}^{j\nu}(\mathbf{p}, \mathbf{q}) O_{a,b}^{i\mu*}(\mathbf{p}, \mathbf{q}) \mathcal{K}_{ab}(\mathbf{p}, \mathbf{q}, \mathbf{B}) \quad (\text{S10})$$

where the overlap function $O_{a,b}^{j\nu}(\mathbf{p}, \mathbf{q}) = \langle u_{a\mathbf{p}+\mathbf{q}/2} | \gamma_{j\nu} | \nu_{b-\mathbf{p}+\mathbf{q}/2} \rangle$ and the kernel function

$$\mathcal{K}_{ab}(\mathbf{p}, \mathbf{q}) = \frac{1 - f(E_a(\mathbf{p} + \mathbf{q}/2)) - f(E'_b(-\mathbf{p} + \mathbf{q}/2))}{E_a(\mathbf{p} + \mathbf{q}/2) + E'_b(-\mathbf{p} + \mathbf{q}/2)} \quad (\text{S11})$$

Here, f is the Fermi distribution function. Note that in the calculation, it is sufficient to consider only the top moiré bands as the pairing energy scale is still much smaller than the moiré bandwidth.

Free energy calculation. In the main text, we have calculated the free energy of the FF pairing $\hat{\Delta}(\mathbf{r}) = \Delta e^{i\mathbf{q}\cdot\mathbf{r}} i\sigma_y$. Here, we present the detailed process. To be convenient, we perform a gauge transform for the mean-field Hamiltonian Eq. (S6): $\Psi_\xi^\dagger(\mathbf{r}) \rightarrow \tilde{\Psi}_\xi^\dagger(\mathbf{r}) e^{-i\frac{1}{2}\mathbf{q}\cdot\mathbf{r}}$. After this gauge transformation, we can obtain a Bogoliubov-de Gennes (BdG) Hamiltonian to describe the FF pairing:

$$H_{BdG}(\mathbf{p}, \mathbf{q}) = \begin{pmatrix} H_0(\mathbf{p} + \frac{\mathbf{q}}{2}) & \Delta i\sigma_y \\ (\Delta i\sigma_y)^\dagger & -H_0^T(-\mathbf{p} + \frac{\mathbf{q}}{2}) \end{pmatrix} \quad (\text{S12})$$

The free energy at every finite momentum \mathbf{q} can then be calculated with

$$\mathcal{F}(\mathbf{q}) = \frac{|\Delta|^2}{U_0} - \frac{1}{\beta} \sum_{\mathbf{p}, n} \ln(1 + e^{-\beta\epsilon_{\mathbf{p}, n}(\mathbf{q})}). \quad (\text{S13})$$

Here, $\epsilon_{\mathbf{p}, n}(\mathbf{q})$ are the eigenenergies of $H_{BdG}(\mathbf{p}, \mathbf{q})$, the attractive interaction strength U_0 can be fixed by the critical temperature T_c .

V. GINZBURG-LANDAU FREE ENERGY FOR A BILAYER SUPERCONDUCTOR UNDER IN-PLANE ORBITAL MAGNETIC FIELDS

Phenomenologically, the Ginzburg-Landau (GL) free energy for a bilayer system under an in-plane orbital magnetic field can be written as

$$\mathcal{F} = \mathcal{F}_c + \mathcal{F}_k + \mathcal{F}_J \quad (\text{S14})$$

$$\mathcal{F}_c = \frac{1}{2A} \left[\int d\mathbf{r} \sum_l (-\alpha_0) |\Delta_l(\mathbf{r})|^2 + \frac{\beta}{2} |\Delta_l(\mathbf{r})|^4 \right], \quad (\text{S15})$$

$$\mathcal{F}_k = \frac{1}{2A} \int d\mathbf{r} \left\{ \frac{1}{2m} \sum_l |\hat{\Pi}_l \Delta_l(\mathbf{r})|^2 - \Gamma [(\Pi_t \Delta_t)^* (\Pi_b \Delta_b) + (\Pi_b \Delta_b)^* (\Pi_t \Delta_t)] \right\}, \quad (\text{S16})$$

$$\mathcal{F}_J = \frac{\lambda_J}{2A} \int d\mathbf{r} |\Delta_t(\mathbf{r}) - \Delta_b(\mathbf{r})|^2 \quad (\text{S17})$$

where $\Delta_l(\mathbf{r})$ is the order parameter layer l , the canonical momentum $\hat{\Pi}_l = (-i\nabla + 2e\mathbf{A}_l)$ with $\mathbf{A}_l = l\frac{d}{2}\mathbf{B} \times \hat{\mathbf{z}}$, $m = 2m^*$ is the mass of Cooper pairings, $\lambda_J \propto \frac{e}{\hbar} N(0)t_c^2$ ($N(0)$ are the density of states near Fermi energy, t_c represents the coupling strength) is the Josephson coupling energy between the two layers, A is sample area. Here, \mathcal{F}_c is the free energy saved by forming Cooper pairing, \mathcal{F}_k contains kinetic energy arising from the intralayer canonical momentum and interlayer canonical momentum mixing of Cooper pairs, Γ denotes the canonical momentum mixing strength between Cooper pair within two layers, \mathcal{F}_J describes the Josephson term which captures the interlayer pairing mixing. Note that due to the giant Ising SOC, we have neglected the paramagnetic free energy.

Next, we simplify the free energy form in the following cases:

(i) The case where the amplitude of the order parameter in each layer has no spatial dependence. In this case, the order parameter becomes $\Delta_t(\mathbf{r}) \equiv |\Delta| e^{i\varphi_t}$ and $\Delta_b(\mathbf{r}) \equiv |\Delta| e^{i\varphi_b}$, and the free energy is simplified as

$$\mathcal{F}(|\Delta|) = -\alpha_0 |\Delta|^2 + \Lambda q_B^2 |\Delta|^2 + \frac{\beta_0}{2} |\Delta|^4 + \lambda_J (1 - \cos(\varphi_t - \varphi_b)) |\Delta|^2, \quad (\text{S18})$$

which is presented in the main text as Eq. (10). Here, $\Lambda = (4\Gamma + \frac{1}{m^*})$. The A_1 pairing with $\varphi_t = \varphi_b$ is thus more favorable so that

$$\mathcal{F}(|\Delta|) = -\alpha_0 |\Delta|^2 + \Lambda q_B^2 |\Delta|^2 + \frac{\beta_0}{2} |\Delta|^4. \quad (\text{S19})$$

For the A_1 pairing, we estimate the critical magnetic field as

$$q_B^2 = \frac{\alpha_0}{\Lambda}. \quad (\text{S20})$$

(ii) The case with layer-antisymmetric FF pairing where $\Delta_t = |\Delta|e^{i\mathbf{q}\cdot\mathbf{r}}$ and $\Delta_b = |\Delta|e^{-i\mathbf{q}\cdot\mathbf{r}}$. Here, we have set $|\Delta_t| = |\Delta_b|$ to save F_J . As discussed in the main text, the favored $\mathbf{q} = (0, 2q_B)$. In this case, the free energy becomes

$$\mathcal{F}(|\Delta|) = -\alpha_0|\Delta|^2 + \frac{\beta_0}{2}|\Delta|^4 + \lambda_J|\Delta|^2. \quad (\text{S21})$$

It can be seen that the layered FF pairing would not pay kinetic energy but exhibit a finite Josephson energy $\lambda_J|\Delta|^2$.

(iii) The case with layer-symmetric FFLO pairing $\Delta_t = \Delta_b = |\Delta_+|e^{i\mathbf{q}\cdot\mathbf{r}} + |\Delta_-|e^{-i\mathbf{q}\cdot\mathbf{r}}$ with $\mathbf{q} = (0, 2q_B)$, $|\Delta_+|^2 + |\Delta_-|^2 = |\Delta|^2$. Note that the pairing within the two layers is identical. In this case, the free energy is deduced as

$$\mathcal{F}(|\Delta|) = -\alpha_0|\Delta|^2 + \frac{\beta_0}{2}(|\Delta|^4 + 2|\Delta_+|^2|\Delta_-|^2) + \frac{2q_B^2}{m^*}|\Delta|^2. \quad (\text{S22})$$

As $\beta_0 > 0$, the free energy is minimized with $|\Delta_+| = |\Delta|, |\Delta_-| = 0$ or $|\Delta_-| = |\Delta|, |\Delta_+| = 0$. Hence, up to the fourth order of the free energy, the favored pairing can only take $\Delta(\mathbf{r}) = |\Delta|e^{i\mathbf{q}\cdot\mathbf{r}}$ or $\Delta(\mathbf{r}) = |\Delta|e^{-i\mathbf{q}\cdot\mathbf{r}}$, which is the $2q_B$ -FF pairing we study in the main text. Then, the free energy of this pairing is simplified as

$$\mathcal{F}(|\Delta|) = -\alpha_0|\Delta|^2 + \frac{\beta_0}{2}|\Delta|^4 + \frac{2q_B^2}{m^*}|\Delta|^2. \quad (\text{S23})$$

Notably, this $2q_B$ -FF pairing exhibits more intralayer kinetic energy but would not exhibit any kinetic energy from the Cooper canonical momentum mixing between two layers. The critical magnetic field of the $2q_B$ -FF pairing is now given by

$$q_B^2 = \frac{m^*\alpha_0}{2}. \quad (\text{S24})$$

Therefore, this $2q_B$ -FF pairing could survive at a higher magnetic field than the uniform pairings if

$$4m^*\Gamma > 1. \quad (\text{S25})$$

We can also infer the FF pairing would be more favorable than the LO pairing in the weak coupling where $\lambda_J \ll 2q_B^2/m^*$.

We clarify here that the phenomenological free energy we present is to give a qualitative understanding of the results of the main text. Some relevant terms in the free energy can be different or some higher-order terms could play a role in the realistic model of twisted bilayer TMDs.

VI. THE LAYER ANTI-SYMMETRIC $2q_B$ FF PAIRING IN AA STACKING BILAYER TMD IN WEAK INTERLAYER COUPLING LIMIT

A. Model

For the AA stacking bilayer TMD without twisting under external magnetic fields \mathbf{B} , the effective low-energy Hamiltonian for valence bands is given by

$$H_0(\mathbf{k} + \epsilon\mathbf{K}) = -\frac{(\hbar\mathbf{k} + e\mathbf{A}\tau_z)^2}{2m^*} - \mu + \epsilon\beta_{so}s_z + t\tau_x. \quad (\text{S26})$$

where $\epsilon = \pm$ denote valley indices, m^* is the effective mass of the valence bands of the monolayer TMD, μ is the chemical potential, β_{so} is the Ising SOC strength, t is the coupling strength between two TMD layers, and Pauli matrices s_i, τ_i operate on the spin-, layer-space, respectively. Notice this Hamiltonian breaks the inversion symmetry since the Ising SOC term $\epsilon\beta_{so}s_z$ is mapped to $-\epsilon\beta_{so}s_z$ under inversion operation. The Zeeman effect from external fields is omitted by assuming a giant Ising SOC $\beta_{so} \gg u_B B$, while the orbital effect from external fields is included in the gauge potential $\mathbf{A} = \frac{d}{2}(\mathbf{B} \times \hat{\mathbf{z}}) = \frac{dB}{2}(\sin\chi\hat{\mathbf{x}} - \cos\chi\hat{\mathbf{y}})$, which is opposite for two layers. Here, d denotes the

interlayer separation, χ characterizes the direction of the magnetic field. Inserting the chosen gauge potential into Hamiltonian (S26), we obtain

$$H_0(\mathbf{k} + \epsilon\mathbf{K}) = -\frac{\hbar^2\mathbf{k}^2}{2m^*} - \frac{\hbar^2}{m^*}(k_B \sin \chi k_x - k_B \cos \chi k_y)\tau_z - \mu' + \epsilon\beta_{so}s_z + t\tau_x \quad (\text{S27})$$

with $l_0 = \sqrt{\hbar/eB}$, $k_B = d/2l_0^2$, $\mu' = \mu + \hbar^2k_B^2/2m^*$. Then the eigenenergies are

$$E_{\epsilon,s,\tau}(\mathbf{k}) = -\frac{\hbar^2\mathbf{k}^2}{2m} - \mu' + \tau\sqrt{t^2 + \left(\frac{\hbar^2k_B}{2m^*}\right)^2(k_x^2 \sin^2 \chi + k_y^2 \cos^2 \chi - k_x k_y \sin 2\chi)} + \epsilon s \beta_{so}. \quad (\text{S28})$$

To be specific, we set the magnetic field to be along the x direction ($\chi = 0$) in the following. The giant SOC can push some bands away from Fermi energy, and in this case, only the top valence bands $E_{+,\uparrow,\tau}(\mathbf{k})$, $E_{-,\downarrow,\tau}(\mathbf{k})$ matter. By projecting the states on these top valence bands, we obtain an effective Hamiltonian as

$$H_0(\mathbf{k} + \epsilon\mathbf{K}) = -\frac{\hbar^2\mathbf{k}^2}{2m^*} - \mu - V(k_y)\tau_z + t\tau_x, \quad (\text{S29})$$

where the chemical potential μ is measured from the valence band top, the orbital field induced term $V(k_y) = \hbar v_B k_y$ with $v_B = \hbar k_B/m^*$. Notice the spin and valley are locked in this case: the \mathbf{K} valley is locked as spin-up, while $-\mathbf{K}$ valley is locked as spin-down. With the Hamiltonian (S29), we can obtain single-particle Green's functions for normal states:

$$G_e(\mathbf{k}, i\omega_n) = (i\omega_n - H_0(\mathbf{k}))^{-1} = G_+(\mathbf{k}, i\omega_n) + G_-(\mathbf{k}, i\omega_n) \frac{-V\tau_z + t\tau_x}{\sqrt{t^2 + V^2}}, \quad (\text{S30})$$

$$G_h(\mathbf{k}, i\omega_n) = (i\omega_n + H_0^*(-\mathbf{k}))^{-1} = -G_e^T(-\mathbf{k}, -i\omega_n), \quad (\text{S31})$$

where $V \equiv V(k_y)$ for the compact of notation, $G_{e(h)}(\mathbf{k}, i\omega_n)$ is electron (hole) Green's function, and

$$G_{\pm}(\mathbf{k}, i\omega) = \frac{1}{2} \left(\frac{1}{i\omega - \xi_+(\mathbf{k})} \pm \frac{1}{i\omega - \xi_-(\mathbf{k})} \right) \quad (\text{S32})$$

with $\xi_{\pm}(\mathbf{k}) = \xi_{\mathbf{k}} \pm \sqrt{V^2 + t^2}$, $\xi_{\mathbf{k}} = -\frac{\hbar^2\mathbf{k}^2}{2m} - \mu$, the Matsubara frequency $\omega_n = (2n + 1)\pi k_B T$, and T denotes the temperature.

B. Zero-momentum pairing

Within in the Nambu basis $(\psi_{\mathbf{k}+\mathbf{K},t}, \psi_{\mathbf{k}+\mathbf{K},b}, \psi_{-\mathbf{k}-\mathbf{K},t}^\dagger, \psi_{-\mathbf{k}-\mathbf{K},b}^\dagger)$, it can be found the BDG Hamiltonian is written as

$$H_{BDG}(\mathbf{k}) = (\xi_{\mathbf{k}} + t\tau_x)\rho_z - V(k_y)\tau_z + \Delta\rho_x. \quad (\text{S33})$$

Let us first consider the usual BCS zero-momentum pairing. For zero-momentum pairing, the superconductivity susceptibility is

$$\begin{aligned} \chi^{(2)}(\mathbf{q} = 0) &= -\frac{1}{\beta_{so}} \sum_{n,\mathbf{k}} \text{Tr}(G_e(\mathbf{k}, i\omega_n)\tau_0 G_h(\mathbf{k}, i\omega_n)\tau_0) \\ &= \frac{2}{\beta_{so}} \sum_{n,\mathbf{k}} (G_+(\mathbf{k}, i\omega_n)G_+(-\mathbf{k}, -i\omega_n) + \frac{t^2 - V^2}{t^2 + V^2} G_-(\mathbf{k}, i\omega_n)G_-(-\mathbf{k}, -i\omega_n)) \\ &= -\frac{1}{2\beta_{so}} \sum_{n,\mathbf{k}} \left(1 + \frac{t^2 - V^2}{t^2 + V^2}\right) \left(\frac{1}{i\omega_n - \xi_{\mathbf{k}} - D} \frac{1}{i\omega_n + \xi_{\mathbf{k}} + D} + \frac{1}{i\omega_n - \xi_{\mathbf{k}} + D} \frac{1}{i\omega_n + \xi_{\mathbf{k}} - D}\right) + \\ &\quad \left(1 - \frac{t^2 - V^2}{t^2 + V^2}\right) \left(\frac{1}{i\omega_n - \xi_{\mathbf{k}} + D} \frac{1}{i\omega_n + \xi_{\mathbf{k}} + D} + \frac{1}{i\omega_n - \xi_{\mathbf{k}} - D} \frac{1}{i\omega_n + \xi_{\mathbf{k}} - D}\right) \end{aligned} \quad (\text{S34})$$

Here $\beta_{so} = 1/k_B T$, $D = \sqrt{V^2 + t^2}$. It can be shown

$$\begin{aligned} \chi_0 &= -\frac{1}{\beta_{so}} \sum_{n,\mathbf{k}} \frac{1}{i\omega_n - \xi_{\mathbf{k}} + A} \frac{1}{i\omega_n + \xi_{\mathbf{k}} - B} \\ &= N_0 \log\left(\frac{2e^\gamma \omega_D}{\pi k_B T}\right) + N_0 \psi\left(\frac{1}{2}\right) - \frac{N_0}{2} \left(\psi\left(\frac{1}{2} - \frac{i(A-B)}{4k\pi k_B T}\right) + \psi\left(\frac{1}{2} + \frac{i(A-B)}{4k\pi k_B T}\right)\right), \end{aligned} \quad (\text{S35})$$

where ω_D is the Debye frequency, N_0 denote the density of states. With Eq. S35, Eq. S34 can be simplified as

$$\chi^{(2)} = 2N_0 \log\left(\frac{2e^\gamma \omega_D}{\pi k_B T}\right) + \frac{2\langle V^2 \rangle}{t^2 + \langle V^2 \rangle} \left[N_0 \psi\left(\frac{1}{2}\right) - \frac{N_0}{2} \left(\psi\left(\frac{1}{2} - \frac{i\sqrt{\langle V^2 \rangle + t^2}}{2\pi k_B T}\right) + \psi\left(\frac{1}{2} + \frac{i\sqrt{\langle V^2 \rangle + t^2}}{2\pi k_B T}\right) \right) \right]. \quad (\text{S36})$$

Here $\langle V^2 \rangle = \frac{1}{2} \hbar^2 v_B^2 k_f^2$, $\langle \dots \rangle$ denotes the averaging over Fermi surface. Therefore, the linearized gap equation is

$$\log\left(\frac{T}{T_c}\right) = \frac{\langle V^2 \rangle}{t^2 + \langle V^2 \rangle} \left[\psi\left(\frac{1}{2}\right) - \frac{1}{2} \left(\psi\left(\frac{1}{2} - \frac{i\sqrt{\langle V^2 \rangle + t^2}}{2\pi k_B T}\right) + \psi\left(\frac{1}{2} + \frac{i\sqrt{\langle V^2 \rangle + t^2}}{2\pi k_B T}\right) \right) \right]. \quad (\text{S37})$$

When $\sqrt{\langle V^2 \rangle + t^2} \ll T_c$, near T_c , Eq. S37 gives

$$B_c = \frac{8\pi k_B T_c}{e v_f |\psi^{(2)}(1/2)|} \sqrt{1 - \frac{T}{T_c}}, \quad (\text{S38})$$

where the Fermi velocity $v_f = \hbar k_f / m^*$.

C. $2q_B$ layer-antisymmetric FF pairing in weak coupling limit

Let us consider the finite-momentum pairing case. We show that the layer antisymmetric pairing momentum with $\mathbf{q} = (0, 2k_B)$ at one layer and $\mathbf{q} = (0, -2k_B)$ is at the other layer is more favorable in the weak coupling limit.

We assume the intra-layer pairing is dominant. As shown in Table S1, there are intra-layer pairing channels: A_1 pairing and A_2 pairing. In the presence of an in-plane magnetic field, $\Delta_{A_1,1}$ and $\Delta_{A_2,1}$ will couple with each other. The Landau free energy, up to the second order, is given by

$$F = \frac{1}{2} \sum_{\mathbf{q}} \begin{pmatrix} \Delta_{A_1,1}^* & \Delta_{A_2,1}^* \end{pmatrix} \begin{pmatrix} \frac{1}{U_0} - \chi_{11}(\mathbf{q}) & -\chi_{12}(\mathbf{q}) \\ -\chi_{21}(\mathbf{q}) & \frac{1}{U_0} - \chi_{22}(\mathbf{q}) \end{pmatrix} \begin{pmatrix} \Delta_{A_1,1} \\ \Delta_{A_2,1} \end{pmatrix}, \quad (\text{S39})$$

where U_0 denotes the intra-layer interaction strength and the superconductivity susceptibility χ can be written as

$$\chi_{ij}(\mathbf{q}) = -\frac{1}{\beta_{so}} \sum_{n, \mathbf{k}} \text{Tr}[\tau_i G_e(\mathbf{k} + \frac{\mathbf{q}}{2}) \tau_j G_h(\mathbf{k} - \frac{\mathbf{q}}{2}, i\omega_n)] \quad (\text{S40})$$

with $\tau_1 = \tau_0, \tau_2 = \tau_z$. Substitute the single-particle Green's function Eq. S30 and Eq. S31, the superconductivity susceptibility can further written as

$$\chi_{11} = \frac{2}{\beta_{so}} \sum_{n, \mathbf{k}} \left[G_+(\mathbf{k} + \frac{\mathbf{q}}{2}, i\omega_n) G_+(-\mathbf{k} + \frac{\mathbf{q}}{2}, -i\omega_n) + \frac{-V^2 + t^2}{V^2 + t^2} G_-(\mathbf{k} + \frac{\mathbf{q}}{2}, i\omega_n) G_-(-\mathbf{k} + \frac{\mathbf{q}}{2}, -i\omega_n) \right], \quad (\text{S41})$$

$$\chi_{12} = \frac{2}{\beta_{so}} \sum_{n, \mathbf{k}} \frac{V}{\sqrt{V^2 + t^2}} \left[G_+(\mathbf{k} + \frac{\mathbf{q}}{2}, i\omega_n) G_-(-\mathbf{k} + \frac{\mathbf{q}}{2}, -i\omega_n) - G_-(\mathbf{k} + \frac{\mathbf{q}}{2}, i\omega_n) G_+(-\mathbf{k} + \frac{\mathbf{q}}{2}, -i\omega_n) \right], \quad (\text{S42})$$

$$\chi_{22} = \frac{2}{\beta_{so}} \sum_{n, \mathbf{k}} \left[G_+(\mathbf{k} + \frac{\mathbf{q}}{2}, i\omega_n) G_+(-\mathbf{k} + \frac{\mathbf{q}}{2}, -i\omega_n) - G_-(\mathbf{k} + \frac{\mathbf{q}}{2}, i\omega_n) G_-(-\mathbf{k} + \frac{\mathbf{q}}{2}, -i\omega_n) \right]. \quad (\text{S43})$$

After some direct calculations, we obtain

$$\chi_{11}(\mathbf{q}) \approx 2N_0 \log\left(\frac{2e^\gamma \omega_D}{\pi k_B T}\right) + \frac{CN_0 v_f^2 q^2}{32\pi^2 k_B^2 T^2} + \frac{CN_0 \langle V^2 \rangle}{4\pi^2 k_B^2 T^2} \quad (\text{S44})$$

$$\chi_{12}(\mathbf{q}) \approx -\frac{CN_0 v_B v_f k_f q_y}{8\pi^2 k_B^2 T^2} \quad (\text{S45})$$

$$\chi_{22}(\mathbf{q}) \approx 2N_0 \log\left(\frac{2e^\gamma \omega_D}{\pi k_B T}\right) + \frac{CN_0 v_f^2 q^2}{32\pi^2 k_B^2 T^2} + \frac{CN_0 \langle V^2 \rangle + t^2}{4\pi^2 k_B^2 T^2}, \quad (\text{S46})$$

where $\langle V^2 \rangle = \frac{1}{2} v_B^2 k_f^2$, $C = \psi^{(2)}(\frac{1}{2})$.

In the weak coupling limit $t \rightarrow 0$, the Landau free energy is

$$\begin{aligned}
F &\approx \sum_{\mathbf{q}} \begin{pmatrix} \Delta_{A_1,1}^* & \Delta_{A_2,1}^* \end{pmatrix} \left[\left(N_0 \log\left(\frac{T}{T_c}\right) - \frac{CN_0 v_f^2 q^2}{64\pi^2 k_B^2 T^2} - \frac{CN_0 v_B^2 k_f^2}{16\pi^2 k_B^2 T^2} \right) \begin{pmatrix} 1 & 0 \\ 0 & 1 \end{pmatrix} + \right. \\
&\quad \left. \frac{CN_0 v_B v_f k_f q_y}{16\pi^2 k_B^2 T^2} \begin{pmatrix} 0 & 1 \\ 1 & 0 \end{pmatrix} \right] \begin{pmatrix} \Delta_{A_1,1} \\ \Delta_{A_2,1} \end{pmatrix} \\
&= \sum_{\mathbf{q}} \lambda_1 |\Delta_1|^2 + \lambda_2 |\Delta_2|^2,
\end{aligned} \tag{S47}$$

where $\Delta_{1,2} = \Delta_{A_1,1} \pm \Delta_{A_2,1}$, $\lambda_{1,2} = N_0 \log\left(\frac{T}{T_c}\right) - \frac{CN_0 v_f^2 q^2}{64\pi^2 k_B^2 T^2} - \frac{CN_0 v_B^2 k_f^2}{16\pi^2 k_B^2 T^2} \pm \frac{CN_0 v_B v_f k_f q_y}{16\pi^2 k_B^2 T^2}$. The critical temperature is given by $\min(\lambda_1, \lambda_2) = 0$. This gives

$$N_0 \log\left(\frac{T}{T_c}\right) - \frac{CN_0}{16\pi^2 k_B^2 T_c^2} \left[\left(\frac{q_y v_f}{2} - \text{sgn}(q_y) v_B k_f\right)^2 + \frac{q_x^2 v_f^2}{4} \right] = 0. \tag{S48}$$

The critical temperature T_c is maximized when $q_x = 0, q_y = \text{sgn}(q_y) 2v_B k_f / v_f$. It is easy to see $q_y = \pm 2k_B$ with $v_B = \hbar k_B / m, v_f = \hbar k_f / m$. And hence, in weak coupling limit $t \rightarrow 0$, the finite-momentum pairing $\Delta_1(\mathbf{q}) = \langle c_{\mathbf{K}+\mathbf{k}+\mathbf{q}/2,+}^\dagger c_{-\mathbf{K}-\mathbf{k}+\mathbf{q}/2,+}^\dagger \rangle$ with $\mathbf{q} = (0, 2k_B)$ and $\Delta_2(\mathbf{q}) = \langle c_{\mathbf{K}+\mathbf{k}+\mathbf{q}/2,-}^\dagger c_{-\mathbf{K}-\mathbf{k}+\mathbf{q}/2,-}^\dagger \rangle$ with $\mathbf{q} = (0, -2k_B)$ are stabilized.